Available online at www.sciencedirect.com
SCIENCE DIRECT®
International Journal of Heat and Mass Transfer 47 (2004) 3877–3887
International Journal of HEAT and MASS TRANSFER
www.elsevier.com/locate/ijhmt

Gas flow in a long microchannel ☆

Shou-Shing Hsieh *, Huang-Hsiu Tsai, Chih-Yi Lin, Ching-Feng Huang, Cheng-Ming Chien

Department of Mechanical and Electro-Mechanical Engineering, National Sun Yat-Sen University, Kaohsiung, Taiwan 80424, People's Republic of China

Received 10 April 2003; received in revised form 11 March 2004

Abstract

An experimental and theoretical study of low Reynolds number compressible gas flow in a microchannel is presented. Nitrogen gas was used. The channel was microfabricated on an oxidized silicon wafer and was 50 μm deep, 200 μm wide and 24,000 μm long. The Knudsen number ranged from 0.001 to 0.02. Pressure drop at inlet and exit of the channel were measured and friction factor constant ratios were calculated at different mass flow rates in terms of *Re*. The results were found in good agreement with those predicted by analytical solutions in which a 2-D continuous flow model with first slip boundary conditions are employed and solved by a perturbation method with a proposed new complete momentum accommodation coefficient σ. Consequently, using slip boundary conditions, one can well predict the mass flow rate as well as inlet/exit pressure drop and friction factor constant ratio for a three-dimensional physical system.

1. Introduction

The field of MEMS is a rapidly emerging technology, where new potential applications are continuously being developed. Microair vehicles, microrobots and nanosatellites are examples of such systems. Moreover, microfabricated channels may be used for integrated cooling of electronic circuits [1] and Joule–Thomson cryo-coolers for infrared detectors and diode lasers [2]. The characteristic length scales that govern the energy and momentum transfer between microelectromechanical systems (MEMS) and their environments are typically on the order of microns. MEMS are often operated in gaseous environments at standard conditions where the molecular mean free path is approximately 70 nm.

As the value of Knudsen number increases, rarefaction effects [3] becomes more important and thus pressure drop, shear stress, heat flux, and corresponding mass flow rate cannot be predicted from flow and heat transfer based on the continuum hypothesis. On the other hand, the gas acceleration occurs due to density variations, which results in a higher friction and pressure drop.

Peiyi and Little [4] measured the friction factors for the flow of gases in mini channels with 130–200 μm wide. Gaseous flow in two-dimensional (2-D) micromachined channels with a Cartesian geometry for various Knudsen numbers was studied by Harley et al. [5] for both experimental and analytical study on rarefied flow. Araki et al. [6] measured friction factors of helium and nitrogen flows in three different microchannels with hydraulic diameters of 3–10 μm. A reduced friction factor was found in a trapezoidal cross section microchannel due to rarefaction effect. However, an friction factor increase was found in a triangular channel because of a possible secondary flow effect.

So far, to the authors' best knowledge and experience, the theoretical and numerical study in gaseous microchannels are all for two-dimensional either on

☆ Part of this work was presented at the first ASME conference on microchannels and minichannels, April 24–25, 2003, Rochester, New York, USA.

* Corresponding author. Tel.: +886-7-5252000x4215; fax: +886-7-5254215.

E-mail address: sshsieh@mail.nsysu.edu.tw (S.-S. Hsieh).

0017-9310/$ - see front matter © 2004 Elsevier Ltd. All rights reserved.
doi:10.1016/j.ijheatmasstransfer.2004.03.027

Nomenclature

A	channel cross section, μm^2
C	a constant in Eq. (24)
C_1	friction constant for fRe
C^*	friction factor constant ratio
c	sonic speed, m/s
D_h	hydraulic diameter of the channel, $4A/p$ μm
f	Darcy's friction factor unless otherwise stated
f_F	Fanning's friction factor
f_t	theoretical friction factor
H	height of the channel, μm
K	Knudsen number, λ/D_h
L	length of the channel, μm
Ma	local Mach number
$\dot{m}$	mass flow rate, mg/s
O	order of magnitude
P'	local pressure except for P_i and P_o, MPa
p	wetted perimeter, μm
R	gas constant, J/(mg K)
Re	Reynolds number based on the hydraulic diameter of the channel
T	temperature, K
u	streamwise (x-direction) velocity, m/s
$\bar{u}$	averaged streamwise velocity from inlet to outlet of the channel, m/s
v	transverse (y-direction) velocity, m/s
W	width of the channel, μm
x	streamwise direction (axis) and distance, μm
y	transverse direction (axis) and distance, μm

Greek symbols

γ	specific heat ratio
ϵ	perturbation variable, H/L
μ	absolute viscosity, N s/m^2
λ	mean free path, μm
ρ	local density of fluid, mg/m^3
$\bar{\rho}$	average density of fluid, mg/m^3
σ, σ_v	complete and tangential momentum accommodation coefficient, respectively

channel cross section (e.g. yz plane with x as flow direction) or on channel midplane (xy plane). In addition, for gaseous microchannel flows modeling, most studies have assumed the momentum accommodation coefficient at wall like σ to be unity. However, several studies have also shown that σ seems no longer being a constant and not solely related to specular reflection.

In this paper, we present experimental data and analytical predictions of compressible channel flow. Although a 2-D parallel plate flow system was still used for prediction, the present tangential momentum accommodation coefficient (σ_v) was obtained from experimental results rather than conventionally assumed a value of 1. Moreover, evaluations of 2-D analytical predictions to approximate a 3-D real system were also made. The pressure drop for the flow of nitrogen gas in a long microchannel fabricated on an oxidized silicon wafer using photolithographic techniques was measured. The objective of this study is to broaden our fundamental understanding for this important emerging field of microfluidics especially in a quite long channel where the effects of the inlet and outlet are negligible.

2. Device design and channel preparation

2.1. Design

The experimental data obtained have been used in the design of a microchannel device for microelectronics cooling. In this section, we describe the design, fabrication process, and actual flow loop of a microchannel device. The design concept tested here can be further developed and incorporated into a microelectronic cooling system. A microchannel was etched in a silicon plate and then a Pyrex glass (7740) where holes were made for the flow inlet and exit was anodically bonded on the top of the plate. The microchannel used has a dimension of $200\times50\times24{,}000$ μm^3 with the aspect ratio of 0.25 (height/width). A schematic diagram of the device along with relevant dimensions is shown in Fig. 1.

2.2. Channel preparation

Although the channel formation is standard micromaching technique, we thought that it is still worthy mentioning especially in a traditional and classical heat and fluid flow related journal. The ultraviolet (UV) exposed region of a photosensitive oxidized silicon wafer is crystallized after thermal treatment and can be etched anisotropically. The fabrication process was divided into two parts. The first part is the silicon etching process. The silicon wafer for the fabrication process is 100 mm diameter, P-type, orientation 1 1 0, and thickness 525 ± 25 μm. The second part is the Pyrex glass drilling process and anodic bonding between silicon and Pyrex glass.

Subsequent fabrication is depicted in Fig. 2. To produce the present channel, an (1 1 0) oriented oxidized silicon wafer, its information listed in Table 1, was firstly thoroughly cleaned with acetone, propane, methanol,

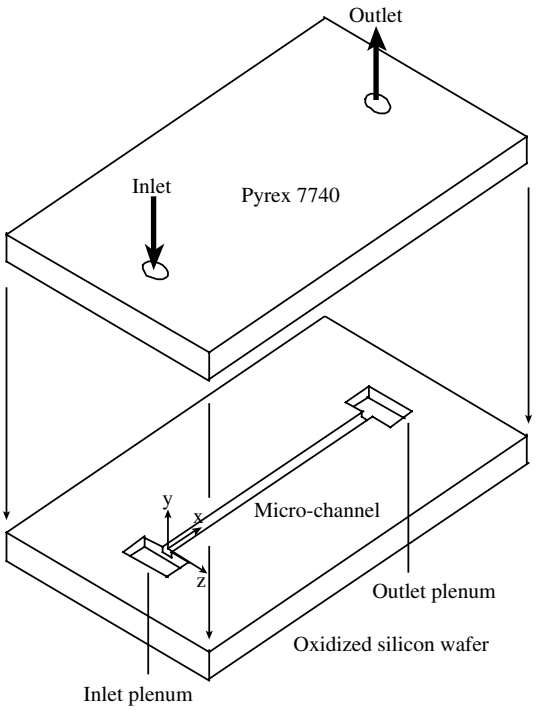

Fig. 1. Close-up view of the present microchannel.

and finally, deionized water. After rinsing, the wafer was treated with a sulfuric and hydrogen peroxide solution to remove any metal or other inorganic contamination from the wafer surface. The wafer was then spinned a thin positive photon resistant and AZ4210 PR was formed on top of the wafer with a thickness of 1.15 μm. The PR pattering conditions is also listed in Table 1. A soft bake process was done after PR layer quality examination was made. Once the above process had done, an UV light (intensity: 40 mW/cm^2) about 365 nm to the photon resistant layer was exposed and then, the mask pattern translated to the photon resistant layer. After developing, the oxide was removed from the channel using HF for 15 min, and cleaned with deionized water. Then, the wafer was subject to a KOH etching solution (~30 wt.%) for varied time at a temperature of 95 °C for different channel depths with an etching rate up to 1.33 μm/min anisotropically. The microchannel was fabricated and, then the oxide was removed again by HF solution, and the structure as well as surface condition was inspected by a microscope and a surface profilemeter (Alpha-Step).

Finally, a 525 μm thick clear Pyrex cover slip was bonded on the top of the wafer to form the closed channel. The geometry configuration of the channel allowing an accuracy less than ±1% and the roughness of the channel along its center with the surface profilemeter with a relative (wrt channel hydraulics diameter) surface roughness less than 0.5% wrt channel height were measured. The relevant geometry dimensions of the resultant microchannel are presented in Table 2.

3. Experimental apparatus and procedure

A schematic diagram of the experiment setup is shown in Fig. 3 in which the device is clamped in a fixture with an internal O-ring to seal the inlet and outlet. Fig. 4 is a photograph of the present microchannel and test loop. Nitrogen (N_2) gas was supplied and controlled from a pressurized cylinder with a regulator (Tescom Co.), and flowed through a mass flow controller (MKS Instruments Inc.), two particle filters (TEM Co.; one is 0.5 μm and one is 0.003 μm), passed two pressure transducers (Granville-Phillips 354; 5×10^{-2}–1×10^{-9} Torr) and two thermistors through the test section at inlet pressure of up to 3.45 bars. The test section inlet was connected to a mass flow meter (MKS Instruments Inc.) having a flow rate range of 0.006–0.321 mg/s for the present flow rate measurements. The accuracy of the mass flow rate measurements is within 3.5%. Noting that prior to N_2 gas flow in, the loop was vacuumed by an vacuum pump (Varian EO50/60) and maintained at 10^{-3} Torr.

Due to the unavailability of appropriate sensors for inside measurements, both pressures and temperatures were measured outside the test section. Pressure drop between the upstream and downstream pressure measurements was measured with an accuracy less than ±1%. Pressure losses in the fittings and feeding lines other than the microchannel are estimated to be a small fraction of the total pressure drop. The temperatures were measured with miniature thermistors at both the inlet and outlet of the test section. The gas entering the test section were at thermal equilibrium with surrounding, and their temperature (≈300 K) was determined with an accuracy of ±0.05 °C. The flow provided by the upstream reservoir was found very stable flowing into the microchannel under continuous operation for up to four hours. The microfilter used was to prevent fluctuations and channel blockage caused by trapped particles. The uncertainties for the relevant flow parameters and variables are tabulated in Table 3. All the measurement devices were connected to an IBM PC for data acquisition and processing.

The present experiments were performed under steady state channel in a clean room, University Microsystem Research Laboratory, where the ambient temperature is controlled at 300 K. The flow was considered to be steady state when the pressure drop measured cannot be changed within 5 min or the change rate is constant for at least 2 min. Each case was repeated at least two times. It shows that it took a longer time for a slower flow rate to reach a steady state.

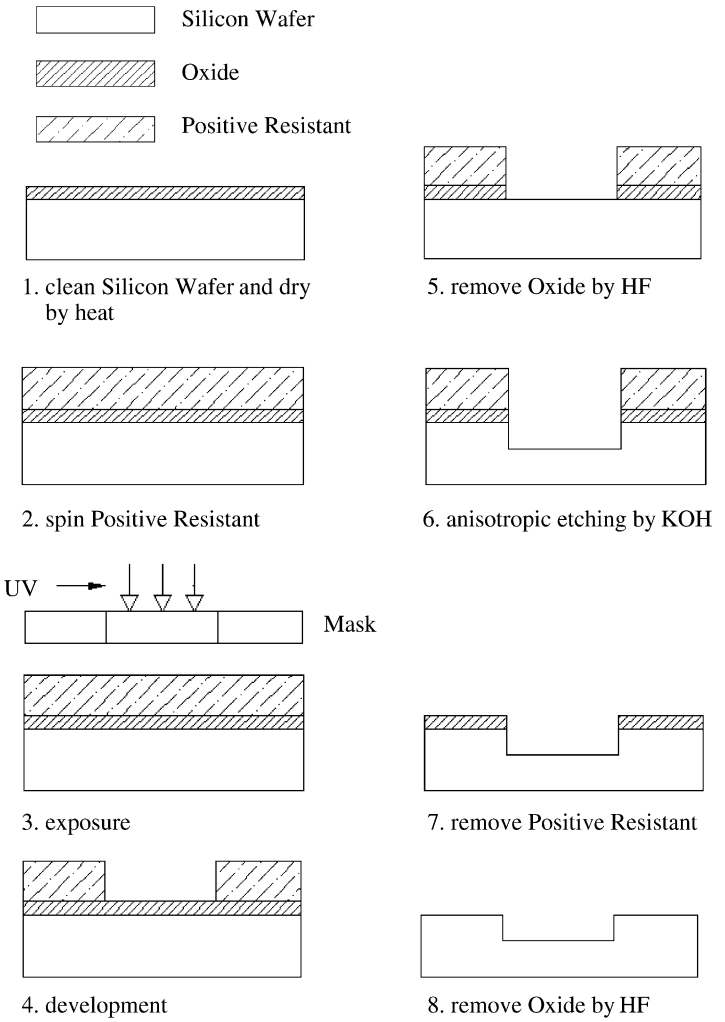

Fig. 2. Fabrication process of the microchannel.

4. 2-D analysis and flow variables calculations

Following Arkilic et al. [7], consider 2-D flow, neglecting variations in the z-direction, the flow is steady, isothermal, compressible, slip flow (i.e., $K = 0.01$–0.1; actually, it will be found $K < 0.02$ for the present study).

Navier–Stokes

$$\rho\left(u\frac{\partial u}{\partial x}+v\frac{\partial u}{\partial y}\right) = -\frac{\partial P'}{\partial x}+\mu\left[\frac{\partial^2 u}{\partial x^2}+\frac{\partial^2 u}{\partial y^2}+\frac{1}{3}\left(\frac{\partial^2 u}{\partial x^2}+\frac{\partial^2 v}{\partial x\,\partial y}\right)\right] \tag{1}$$

$$\rho\left(u\frac{\partial v}{\partial x}+v\frac{\partial v}{\partial y}\right) = -\frac{\partial P'}{\partial y}+\mu\left[\frac{\partial^2 v}{\partial x^2}+\frac{\partial^2 v}{\partial y^2}+\frac{1}{3}\left(\frac{\partial^2 v}{\partial y^2}+\frac{\partial^2 u}{\partial x\,\partial y}\right)\right] \tag{2}$$

Continuity equation

$$\nabla\cdot(\rho\bar{u}) = 0 \tag{3}$$

The equation of state for an ideal gas

$$P' = \rho RT \tag{4}$$

The momentum equation in a nondimensional form

$$Re\,\widetilde{P}\left(\epsilon\tilde{u}\frac{\partial\tilde{u}}{\partial\tilde{x}}+\tilde{v}\frac{\partial\tilde{u}}{\partial\tilde{y}}\right) = -\frac{\epsilon Re}{\gamma Ma^2}\frac{\partial\widetilde{P}}{\partial\tilde{x}}+\epsilon^2\frac{\partial^2\tilde{u}}{\partial\tilde{x}^2}+\frac{\partial^2\tilde{u}}{\partial\tilde{y}^2} +\frac{1}{3}\left(\epsilon^2\frac{\partial^2\tilde{u}}{\partial\tilde{x}^2}+\epsilon\frac{\partial^2\tilde{v}}{\partial\tilde{x}\,\partial\tilde{y}}\right) \tag{5}$$

$$Re\,\widetilde{P}\left(\epsilon\tilde{u}\frac{\partial\tilde{v}}{\partial\tilde{x}}+\tilde{v}\frac{\partial\tilde{v}}{\partial\tilde{y}}\right) = -\frac{Re}{\gamma Ma^2}\frac{\partial\widetilde{P}}{\partial\tilde{y}}+\epsilon^2\frac{\partial^2\tilde{v}}{\partial\tilde{x}^2}+\frac{\partial^2\tilde{v}}{\partial\tilde{y}^2} +\frac{1}{3}\left(\frac{\partial^2\tilde{v}}{\partial\tilde{y}^2}+\epsilon\frac{\partial^2\tilde{u}}{\partial\tilde{x}\,\partial\tilde{y}}\right) \tag{6}$$

Table 1
The information of wafer and pattern

	Si	Pyrex
Wafer		
Diameter	100 ± 0.01 mm	100 ± 0.01 mm
Thickness	525 ± 25 μm	525 ± 25 μm
Crystallization direction	(1,1,0)	–
Type	P type	–
Electric resistance	3–9 Ω cm	
Surface treatment	SiO_2 1 μm	Two side polished
Molecular weight	28.09	–
Crystallization	Cubic	–
Lattice space, Å	5.43	–
Density at 293 K, g/cm^3	2.329	2.23
Dielectric constant (at 9.37×10^9 Hz)	13	4.60
Melting point, K	1690	–
AZ 4210 PR pattern conditions		
PR coating	AZ 4210	
PR property	Positive	
PR type	Thin film	
Speed	4000 rpm	
Soft bake (90 °C)	1 min 30 s	
UV light wave length	365 nm	
Light intensity	40 mW/cm^2	
Exposure time	7 s	
Development	3 min 30 s	

Table 2
Results of microchannel characterization

Characterization	Dimensions
Channel length L	24 mm
Channel depth H	50 μm
Channel width W	200 μm
Silicon wafer thickness H_s	525 μm
Pyrex glass thickness H	525 μm
Total thickness of the test section H	1.05 mm
Pyrex glass width W_g	100 mm
Channel hydraulic diameter	80 μm
Channel surface roughness Ra	1.47 μm
Outer diameter of the inlet/outlet tube	1.50 mm
Inner diameter of the inlet/outlet tube	0.61 mm
Thickness of the tube	0.89 mm

where

$$\widetilde{P}=\frac{P'}{P_o},\quad \tilde{u}=\frac{u}{c},\quad \tilde{v}=\frac{v}{c}\quad \tilde{x}=\frac{x}{L},\quad \tilde{y}=\frac{y}{H}$$
$$Ma=\frac{\bar{u}}{c},\quad \tilde{\rho}=\frac{\rho}{\rho_o},\quad \epsilon=\frac{H}{L},\quad \text{and}\quad Re=\frac{\bar{\rho}\bar{u}H}{\mu} \tag{7}$$

The nondimensional continuity equation

$$\epsilon\frac{\partial(\tilde{\rho}\tilde{u})}{\partial\tilde{x}}+\frac{\partial(\tilde{\rho}\tilde{v})}{\partial\tilde{y}}=0 \tag{8}$$

with boundary conditions at $\tilde{y}=\pm\frac{1}{2}$

$$\tilde{u}_{wall}=\sigma K\left.\frac{\partial\tilde{u}}{\partial\tilde{y}}\right|_{wall};\quad \text{where } K \text{ is the Knudsen number} \tag{9}$$

where σ stands for complete momentum accommodation coefficient and was obtained from the experimental results derivations of the present study rather than directly measured, and

$$\tilde{v}|_{wall}=0 \tag{10}$$

Now, let us expand $\tilde{u}$, $\tilde{v}$, $\widetilde{P}$ in powers of ϵ as follows:

$$\tilde{u}=\tilde{u}_0+\epsilon\tilde{u}_1+\epsilon^2\tilde{u}_2+\cdots \tag{11}$$

$$\tilde{v}=\epsilon\tilde{v}_1+\epsilon^2\tilde{v}_2+\epsilon^3\tilde{v}_3+\cdots \tag{12}$$

$$\widetilde{P}=\widetilde{P}_0+\epsilon\widetilde{P}_1+\epsilon^2\widetilde{P}_2+\cdots \tag{13}$$

It is clear from Eq. (8) that the highest order $\tilde{v}$ term that is required to satisfy the differential continuity equation is in $O(\epsilon)$.

With kinetic gas theory, the Knudsen number can be written as

$$K=\sqrt{\frac{\pi\gamma}{2}}\frac{Ma}{Re} \tag{14}$$

In our case, let us consider $Ma=O(\epsilon)$ and $Re=O(\epsilon)$, then $\frac{Re}{Ma^2}=O(1/\epsilon)$.

This gives the y-momentum equation for $O(1/\epsilon)$, i.e.,

$$\widetilde{P}=\widetilde{P}(\tilde{x}) \tag{15}$$

and x-momentum equation that at $O(1)$ is

$$\frac{\epsilon Re}{\gamma Ma^2}\frac{d\widetilde{P}}{d\tilde{x}}=\frac{\partial^2\tilde{u}}{\partial\tilde{y}^2} \tag{16}$$

After integrating Eq. (16) twice and applying the above boundary conditions, one may obtain the following expression:

$$\tilde{u}_o=-\frac{\epsilon Re}{8\gamma Ma^2}\left(\frac{d\widetilde{P}}{d\tilde{x}}\right)[1-4\tilde{y}^2+4\sigma K_o] \tag{17}$$

Substituting $\tilde{u}$ into the continuity equation of Eq. (8) and integrating the resultant equation in y, one can get

$$\tilde{v}_1=\frac{1}{\widetilde{P}}\frac{\epsilon Re}{8\gamma Ma^2}\left[\left(\frac{1}{2}\right)\left(\frac{d^2(\widetilde{P}^2)}{d\tilde{x}^2}\right)\times\left(\tilde{y}-\frac{4}{3}\tilde{y}^3\right)+4\sigma K_o\tilde{y}\frac{d\widetilde{P}}{d\tilde{x}}\right] \tag{18}$$

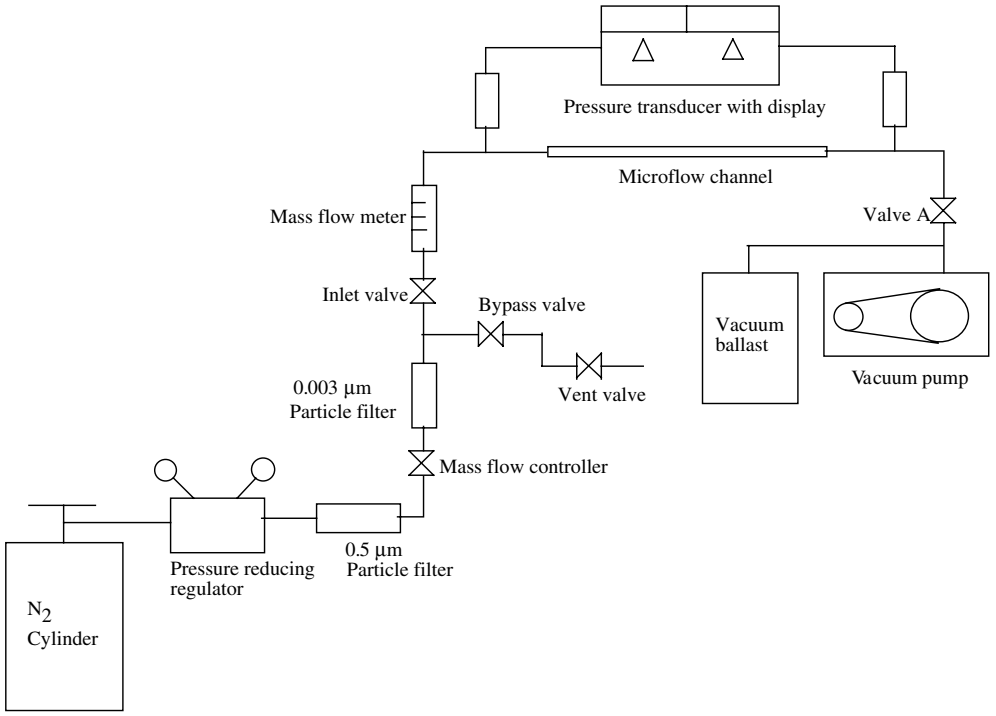

Fig. 3. Experimental setup for microflow measurements.

Since the wall-normal velocity must vanish, i.e.,

$$\frac{\mathrm{d}^2(\widetilde{P}^2)}{\mathrm{d}\tilde{x}^2} + 12\sigma K_\mathrm{o}\frac{\mathrm{d}\widetilde{P}}{\mathrm{d}\tilde{x}} = 0 \tag{19}$$

where $\widetilde{P}$ = local dimensionless pressure, and it gives (see Appendix A)

$$\widetilde{P}(\tilde{x}) = -6\sigma K_\mathrm{o} + \sqrt{(6\sigma K_\mathrm{o})^2 + (1+12\sigma K_\mathrm{o})\tilde{x} + (P^2 + 12\sigma K_\mathrm{o} P)(1-\tilde{x})} \tag{20}$$

where P stands for the pressure ratio of $P_\mathrm{i}/P_\mathrm{o}$. Finally, the dimensional mass flow rate for the given inlet/outlet pressure can be found by multiplying the density ρ to Eq. (17) and integrating across the channel and evaluating at $\tilde{x} = 1$, results in

$$\dot{m} = \frac{H^3 W P_\mathrm{o}^2}{24\mu LRT}\left[P^2 - 1 + 12\sigma K_\mathrm{o}(P-1)\right] \tag{21}$$

After simplifying,

$$\dot{m} = \frac{H^3 W P_\mathrm{o}^2}{24\mu LRT}\left[\left(\frac{P_\mathrm{i}}{P_\mathrm{o}}\right)^2 - 1 + 12\sigma K_0\left(\frac{P_\mathrm{i}}{P_\mathrm{o}} - 1\right)\right] \tag{22}$$

where P_o (P_i) is the dimensional outlet (inlet) pressure. H, W, and L are the channel height, width, and length, respectively. While, T, μ, and R are the fluid temperature, molecular viscosity, and specific gas constant. K_o is the outlet Knudsen number.

5. Results and discussion

The analytical results based on 2-D perturbation of a continuous flow model with first order slip boundary conditions and a new σ proposed were obtained in which pressure drops with different mass flow rates (also in terms of Re) were calculated to approximate the present 3-D rectangular microchannel of $200\times50\times24{,}000$ μm^3 with varied $0.001 < K < 0.02$. In addition, pressure drop measurements were also made at inlet and outlet of the channel at Reynolds number range of $2.6 < Re < 89.4$ for an isothermal (≅300 K) flow and compared with the analytical predictions.

5.1. 2-D analytical solutions

Table 4 depicts the inlet Knudsen number (K) and inlet Mach number (Ma) values vs the pressure ratio ($P_\mathrm{i}/P_\mathrm{o}$). For instance, for N_2 gas at 2.7 kPa inlet pressure with an inlet $K \cong 0.0248$. It can be seen that the K is quadratically decreased as inlet pressure increases as one would expect. However, the Mach number goes the other way around with a slow linear increase. Also included in Table 4 are the inlet density values.

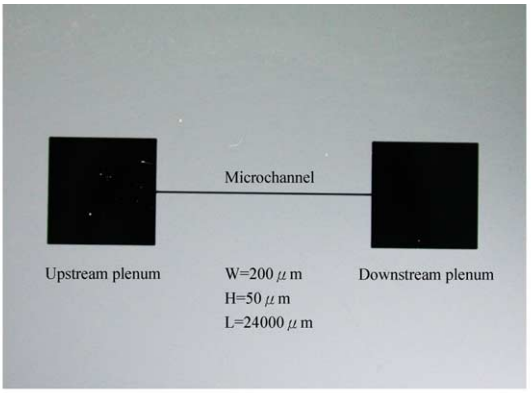

(a)

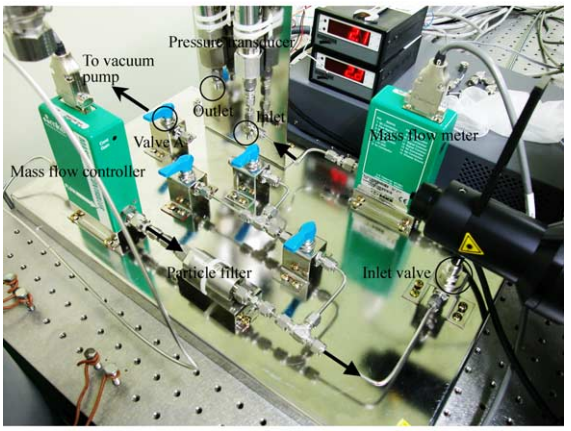

(b)

Fig. 4. Photograph of experimental setup. (a) Photograph of microchannel and (b) photograph of test loop.

Table 3
Uncertainties of geometric dimensions and relevant parameters

Geometric and parameters	System error	Random error
Q (cm^3/min)	±0.5%	±3.5%
ΔP (kPa)	±0.1%	±0.6%
Re	±0.53%	±0.93%
f	±0.72%	±1.1%
$\Delta P/\Delta L$ (kPa/cm)	±0.1	±0.6
T (°C)	±0.05 °C	±0.07 °C

Dimensional mass flow rates calculated based on Eq. (22) with inlet pressure ratios are listed in Table 4 which is in fair agreement with those from experiments within an average deviation less than 15%. It is expected that the mass flow rate gradually increases as the inlet pressure increases. Fig. 5 shows the Knudsen and Mach number distribution along the downstream distance. It is found that both number increase along the channel and reach the maximum at the channel outlet.

Local pressure distribution shown in Fig. 6 indicates a moderate pressure drop in the present quite long microchannel for different mass flow rate. Since the pressure drop measurements were only made at inlet/exit of the channel, the detailed distribution comparison is not possible. But, these values calculated at inlet and exit, and plotted in Fig. 6 should not deviate from those measurements as one would expect. Generally speaking, pressure drop in the present microchannel is caused by shear stress and gas acceleration. However, the pressure drop by gas acceleration is quite small (<2%) in this study. The experimental results were used to make comparisons with those of the analytical solutions as stated before. The comparisons were made under the conditions setup as close as possible. Furthermore, due to the change in local density, the nonlinear distribution for ΔP was found. Even though the Mach number at outlet is quite low as compared to the conventional theory ($Ma \leqslant 0.3$) for an in compressible flow, the compressibility is still effective. The pressure drop increases as the mass flow rates increase. However, the ΔP values of the microchannel is consistently smaller than those in conventional larger channels (not shown). Fig. 7(a) shows the downstream streamwise velocity at centerline for $Re = 3.2$. The velocity is obviously accelerated because of a local bulk density of N_2 decrease due to a low local pressure there. Consequently, the flow seems never reached fully developed. Fig. 7(b) shows streamwise velocity (u) distribution spanned across the y-axis and the traditional parabolic curves are still existed. Noting that with the present slip flows at wall, the velocity is no longer to be zero near the wall.

5.2. Microflow experimental results and comparisons

The hydraulic diameter of the present long channel is 80 μm and the experiments were conducted with various flow rates which yield Re up to 89.4. In each case, the flow rate was kept constant and the pressure drop required to force the gas through the microchannel was measured. The pressure drop per channel length for all the cases (i.e., different Re) can be plotted against the downstream distance and correlated as a function of Re (not shown).

Following Araki et al. [6], Li and Ma [8] and Qu et al. [9], at a specified Reynolds number the friction factor constant ratio C^* is defined as

$$C^* = f/f_t \tag{23}$$

C^* can also be found [6] and written as

$$C^* = \frac{1}{(1 + C\overline{K})} \tag{24}$$

Table 4
Inlet/outlet pressures, pressure ratios, inlet Knudsen number, inlet Mach number, inlet density, calculated mass flow rates (analytical) and mass flow rates (measurement) with deviations

Inlet pressure, P_i (kPa)	Pressure ratio, (P_i/P_o)	Outlet pressure, P_o (kPa)	Knudsen number, K	Mach number, M	Density, ρ (mg/m^3)	Mass flow rate based on 2-D analytical solution (mg/s)	Mass flow rate based on experimental results (mg/s)	Deviations
2.7	3.97	0.68	0.024	0.0013	1200	0.0112	0.0088	0.27
5.4	4.21	1.36	0.01	0.0023	1230	0.0224	0.0215	0.04
14.29	4.35	3.28	0.0046	0.0057	1330	0.0784	0.0617	0.27
27.9	4.56	6.12	0.0024	0.0107	1490	0.1568	0.1320	0.19
40.14	4.62	8.69	0.0017	0.0152	1630	0.2464	0.2134	0.15
51.02	4.74	10.76	0.0013	0.0192	1760	0.3248	0.2971	0.09
64.63	4.91	13.19	0.001	0.0241	1920	0.4368	0.4092	0.07

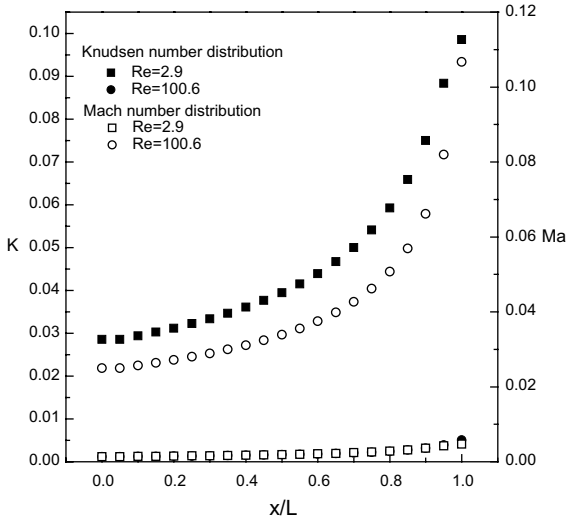

Fig. 5. Knudsen number and Mach number distribution along downstream distance.

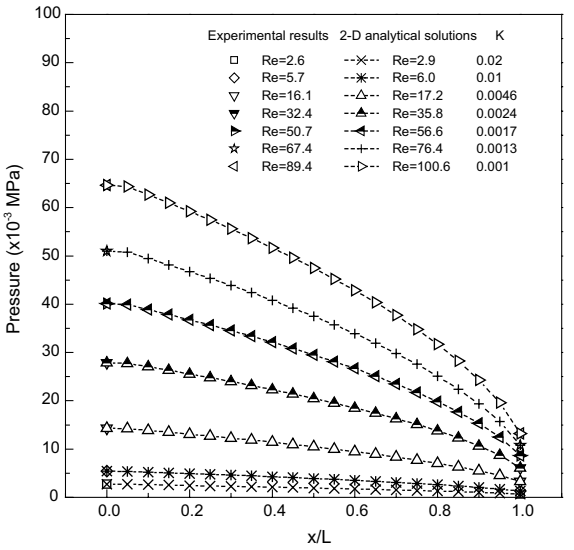

Fig. 6. The comparison of pressure drop with experimental results and 2-D analytical solutions.

for various channel geometries where f was obtained from experiments and analytical results where $\overline{K}$ is an average of inlet and outlet Knudsen number. The theoretical values (f_t) of Darcy friction factor for the present parallel plate and rectangular channel with aspect ratio 0.25 are 96 and 72.9, respectively. σ in Eq. (9) can be found based on Arkilic [10] through the present mass flow rate measurements. The σ obtained (see Appendix B) in the present study is a function of outlet Knudsen number [10] which was shown in Fig. 8. It can be seen that the complete momentum accommodation coefficient σ slowly increases with K_o ($\sim K_o^{0.334}$) due perhaps to rarefaction effect with the corresponding σ_v, tangential momentum accommodation coefficients, varied in a range of 0.3–0.7.

Figs. 9 and 10 show such comparisons among those results from experiments, theoretical slip/nonslip solutions, and 2-D analytical solutions for f of Darcy's and Fanning's, respectively. In spite of quite a few data used for ΔP measurement. But, nevertheless, the results can still be useful and can be considered supplementary to the existing documentation. The corresponding f for present rectangular channel was calculated and correlated in a form of $f\,Re = C_1$ which is shown in Fig. 9 where the friction factors were plotted against Re. It is clearly seen that the present results could be correlated in a traditional form like $f\,Re = C_1$, but C_1 seems no longer to be a constant with a very small uncertainty of ±2%. In this case, a smaller C_1 (≈48 with $Re^{-1.02}$) for Darcy friction factor was found as compared to that of 72.9 (theoretical value with nonslip for an aspect ratio 0.25); while the experimental measurement distribution

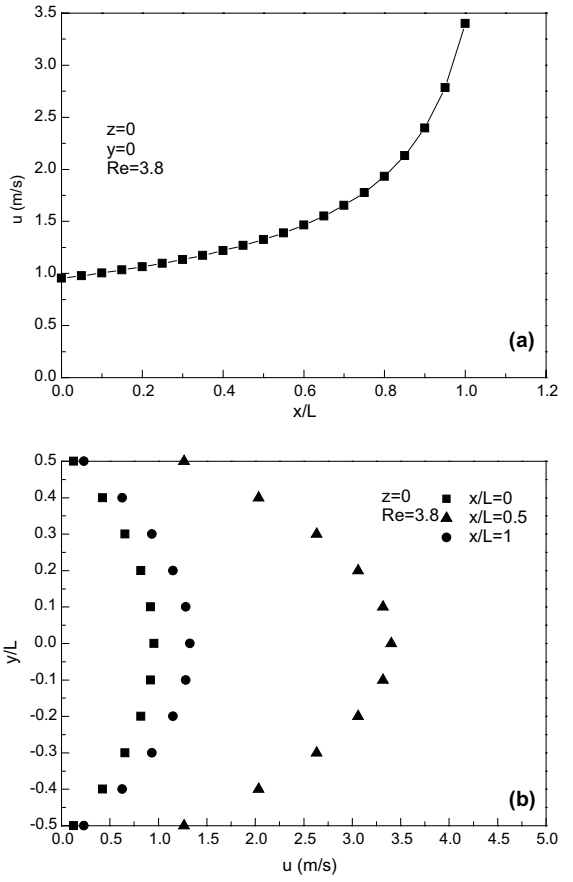

Fig. 7. Velocity distributions (calculated) along the (a) streamwise and (b) transverse direction.

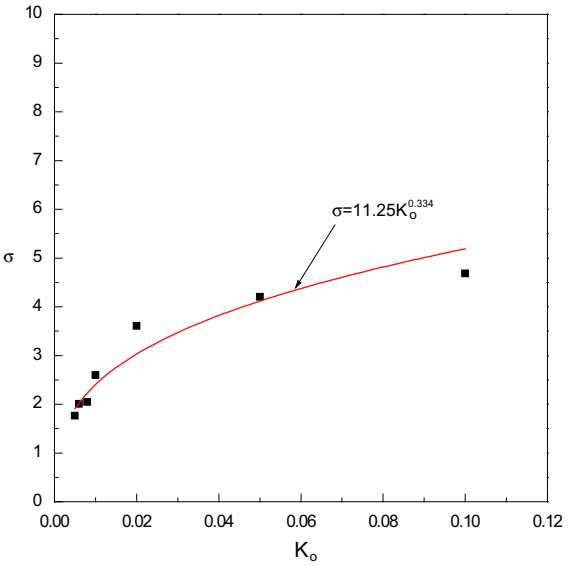

Fig. 8. σ vs K_o.

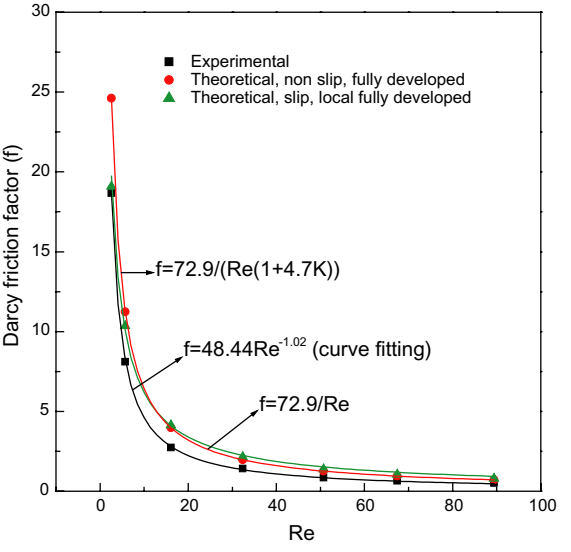

Fig. 9. f (Darcy) vs Re in a rectangular microchannel with aspect ratio 0.25.

and values are very close to the results with slip conditions at $Re < 10$. Moreover, this result is in good agreement with that (≈49) of Harley and Bau [11]. It indicates that the pressure drop in a microchannel with the same operating condition would have a smaller value than that in a conventional channel. But, such deviation becomes small as Re increases. The analytical solutions from 2-D modeling and simulation is shown in Fig. 10. The coefficient of Fanning friction factor compares to those of theoretical values for an infinite parallel plate with slip and nonslip boundary condition, respectively. Again, the deviation becomes negligible as Re increases.

Furthermore, in both Figs. 9 and 10, $f\,Re$ results obtained from the incompressible nonslip flow theory for rectangular channel ($C_1 = 72.9$, Darcy) as well as parallel plate channel ($C_1 = 24$, Fanning) for fully developed flow were compared to those of compressible slip flow with "local fully developed" assumption results $f = 72.9(24)/Re(1 + CK)$ from Navier–Stokes equation plus slip flow boundary conditions with a new C value ($=4.7$) instead of the conventional value of 6, respectively, for a rectangular channel (parallel plate). This new C was derived from the plot of C^* vs $\overline{K}$ for Eq. (24) (not shown). The deviation is obvious due to gas acceleration and it was caused partly by the compressibility of the gas under study and partly by the real cases departure from "fully developed". In fact, a very close value ($C = 4.08$) was also reported in a previous study for a circular tube [12].

In the present channel, in spite of a smaller Ma, the order of magnitude $O(10^{-2})$, the compressibility effect is

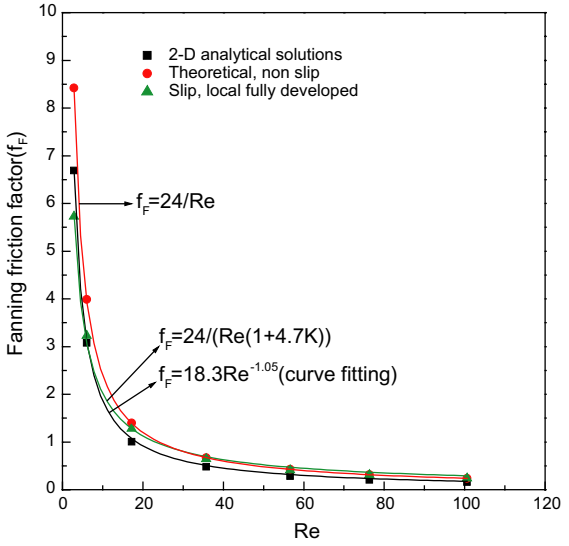

Fig. 10. $f(f_F)$ vs Re for a parallel plate.

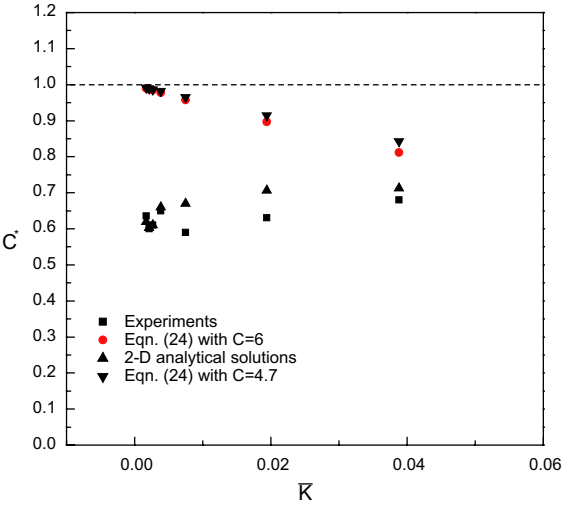

Fig. 11. Friction factor constant ratio, C^*, as a function of average Knudsen number.

still dominated which was assessed by analytical results (ΔP) in Fig. 6 and further by pressure measurements in Fig. 8. This is evidenced by the fact that as the inlet/outlet pressure difference bigger than 10 kPa, the compressibility effects (nonlinear pressure distribution) become significant (for the case $Re \geqslant 16.1$). Again, as reported in Araki et al. [6], the compressibility effects in microchannel can be better described by the pressure drop rather than a Mach number as in conventional theory. Moreover, due to a higher pressure drop and small channel sizes in microflows, rarefaction influence can also be clearly noted. In fact, the product of $C_1 \cong 48$ from the present experiments is smaller than that for larger conventional channels ($C_1 \cong 72.9$). This is because the slip effect at wall due to rarefaction reduced the product of C_1. The finding again confirms the previous studies for trapezoidal and rectangular channels (see, [11] for example).

Fig. 11 shows the C^* calculated from Eq. (23) vs $\overline{K}$. As one can see, C^* for 2-D parallel plate, results from analytical solutions, is very close to the present experiments for a rectangular microchannel of aspect ratio 0.25 within ±10%. Also included in Fig. 11 are the calculations based on Eq. (24) with $C = 6$ (conventional) and $C = 4.7$ (the present study), respectively, for "local fully developed" assumption results. The deviation for all the curves is getting small as $\overline{K}$ increases. Again, the present 2-D approximation was in good agreement for friction factor constant ratio calculation with that of experiments. Moreover, the range of C^* all falls within 0.7–0.6, deviated from the traditional ratio of unity for conventional channels and, consequently, suggests a friction factor reduction (about 30–40%) of the present study.

6. Conclusion

Gaseous flow characteristics of N_2 in a microchannel were studied. A channel of $200 \times 50 \times 24{,}000$ μm^3 with a hydraulic diameter of 80 μm and aspect ratio of 0.25 was fabricated and tested for different mass flow rates in terms of Re ($2.6 \leqslant Re \leqslant 89.4$). The slip effect still exists for the entire inlet Knudsen number range of this study, i.e., $0.001 < K < 0.02$. The major findings can be drawn as follows:

1. The pressure drop exhibits an unusual nonlinear behavior as compared to that in a larger channel due to the compressibility effect. The rarefaction and compressibility effect were both found in the present channel under the present operating conditions. However, the compressibility effect seems smaller.
2. It is found that the pressure drop required is smaller than that in a conventional channel. This finding also coincides with the previous studies.
3. The present analytical results based on a continuous flow model with first slip boundary condition followed by Arkilic et al. [7] for a 2-D parallel plate are found in good agreement with the experimental results for a rectangular 3-D channel of aspect ratio 0.25 under certain conditions and the flow seems never reached fully developed.
4. Based on Arkilic et al. [10] and with the present mass flow rate measurements, the so-called tangential momentum accommodation coefficient, σ_v, was found in the range of 0.3–0.7 for the present N_2 gaseous microchannel flows.

5. A 2-D theoretical study to model and simulate a 3-D rectangular system was found inappropriate as far as friction constant C_1 is concerned. However, the pressure drop as well as mass flow rates and friction factor constant ratios of a 2-D model as stated in remark (3) can predict 3-D system well. In the meantime, a new set of complete momentum accommodation coefficients σ was found through σ_v to be a function of Knudsen number instead of a constant of unity, which might be helpful for future numerical modeling.
6. Both compressibility (even small) and rarefaction effects were experimentally observed for all the *Re* studied. Moreover, when $Re \geqslant 16.1$ the compressibility effect becomes a little bit strong. Again, instead of using *Ma*, the amount pressure drop between inlet/outlet of the microchannel (e.g. >10 kPa) can be more appropriate to describe the compressibility of the microchannel gaseous flow.

Appendix A

Eq. (19) can be rearranged in the following form:

$$\frac{d^2}{d\tilde{x}^2}(\widetilde{P}^2 + 12\sigma K_o \widetilde{P}) = 0 \tag{A.1}$$

Integrating (A.1), one can obtain

$$\widetilde{P}^2 + 12\sigma K_o \widetilde{P} = C_1 \tilde{x} + C_2 \tag{A.2}$$

By using proper boundary conditions

$$\begin{aligned} &\tilde{x} = 1, \qquad \widetilde{P} = 1 \\ &\tilde{x} = 0, \qquad \widetilde{P} = P \end{aligned} \tag{A.3}$$

We can get

$$\begin{aligned} C_1 &= 1 + 12\sigma K_o(1 - P) - P^2 \\ C_2 &= 12\sigma K_o P + P^2 \end{aligned} \tag{A.4}$$

Substitute C_1 and C_2 into Eq. (A.2), it gives

$$\widetilde{P}^2 + 12\sigma K_o \widetilde{P} - [1 + 12\sigma K_o(1 - P) - P^2]\tilde{x} - (P^2 + 12\sigma K_o P) = 0 \tag{A.5}$$

Solving Eq. (A.5) for $\widetilde{P}$, it results in Eq. (20) as follows:

$$\widetilde{P}(\tilde{x}) = -6\sigma K_o + \sqrt{(6\sigma K_o)^2 + (1 + 12\sigma K_o)\tilde{x} + (P^2 + 12\sigma K_o P)(1 - \tilde{x})} \tag{20}$$

Appendix B

The calculations for the value of "σ" can be explained as follows:

Since $\sigma = \frac{2-\sigma_v}{\sigma_v}$, and σ_v can be found based on the following equation [10]:

$$\frac{\dot{m}}{\Delta P} = \frac{H^3 W}{12\mu LRT}\overline{P} + \frac{H^3 W}{2\mu LRT}\left(\frac{2 - \sigma_v}{\sigma_v}\right) K_o P_o$$

where $\dot{m}$: mass flow rate, ΔP: pressure difference $P_i - P_o$, and the average pressure was taken at $\overline{P} = \left(\frac{P_i + P_o}{2}\right)$.

Once we get $\dot{m}$ and P_i from experiments and from a known value of P_i/P_o, and results of K_o, one may obtain σ_v. Finally, by $\sigma = \frac{2-\sigma_v}{\sigma_v}$, one can also get σ.

References

[1] D.B. Tuckerman, Heat transfer microstructures for integrated circuits, 1984, UCRL 53515 Report, Lawrence Livemore National Laboratory, USA.
[2] P. Wu, W.A. Little, Measurement of heat transfer characteristics of the gas flow in fine channel heat exchangers used for microminiature Joule–Thomson refrigerators, Cryogenics 24 (1984) 415–423.
[3] A. Beskok, G.E. Karniadakis, W. Trimmer, Rarefaction and compressibility effects in gas microflows, J. Fluids Eng. 118 (1996) 448–456.
[4] W. Peiyi, W.A. Little, Measurements of friction factors for the flow of gaseous in very fine channel used for micro miniature Joule–Thomson refrigerators, Cryogenics 23 (1983) 273–277.
[5] J.C. Harley, Y. Huang, H.H. Bau, J.N. Zemel, Gas flow in micro-channels, J. Fluid Mech. 284 (1995) 257–274.
[6] T. Araki, M.S. Kim, H. Iwai, K. Suzuki, An experimental investigation of gaseous flow characteristics in microchannels, Microscale Thermophys. Eng. 6 (2002) 117–130.
[7] E.B., Arkilic, K.S. Breuer, M.A. Schmit, Gaseous flow in microchannels, Application of Microfabrication to Fluid Mechanics 1994, Chicago, IL, pp. 57–66.
[8] G.M. Mala, D. Li, Flow characteristics of water in microtubes, Int. J. Heat Fluid Flow 20 (1999) 142–148.
[9] W. Qu, G.M. Mala, D. Li, Pressure-driven water flows in trapezoidal silicon microchannels, Int. J. Heat Mass Transfer 43 (2000) 353–364.
[10] E.B. Arkilic, K.S. Breuer, M.A. Schmidt, Mass flow and tangential momentum accommodation in silicon micromachined channels, J. Fluid Mech. 437 (2001) 29–43.
[11] J. Harley, H. Bau, Fluid flow in micro and sub-micron size channels, IEEE Trans. THO 249-3 (1989) 25–28.
[12] J.M. Li, B.X. Wang, X.F. Peng, The wall effect for laminar flow through microtubes, in: Proceedings ICHMT, Symposium on Molecular and Microscale Heat Transfer in Materials Processing and Other Applications, 1996, pp. 55–65.